6.2   DIRECT OBSERVATION OF THE EVAPORATION OF INTERCEPTED WATER OVER AN OLD-GROWTH FOREST IN THE EASTERN AMAZON REGION

Matthew J. Czikowsky[1]*, David R. Fitzjarrald[1], Ricardo K. Sakai[1], Osvaldo L. L. Moraes[2],
Otávio C. Acevedo[2], and Luiz E. Medeiros[1]
(1) University at Albany, State University of New York, Albany, New York
(2) Universidade Federal de Santa Maria, Santa Maria, RS, Brazil

1. INTRODUCTION

Interception of rainfall by the forest canopy and the subsequent re-evaporation into the atmosphere constitute an important part of the hydrological balance over forests. On an annual basis in a forest environment, transpiration is the dominant component of evapotranspiration (ET), followed by interception evaporation and then bare-soil and litter evaporation. However, during and following transient precipitation events, interception exceeds transpiration as the dominant component of ET, resulting in a shift in the hydrological balance. During the process of interception evaporation, the leaves are wet, so the stomatal resistance goes to zero. Under such conditions, when surface (physiological) controls are removed, very enhanced rates of evaporation of intercepted water are to be expected from forests compared to shorter vegetation, in all climatic zones (Newson and Calder 1989). Evaporation from a wet forest canopy can proceed at a greater rate than a dry one, up to five times that of the transpiration of surface-dry vegetation (Hewlett 1982). During interception-loss periods, two-thirds of total ET can be evaporation of intercepted water from the leaf surfaces (Stewart 1977).

An appreciable fraction of water vapor in the Amazon is recycled through ET, with 25 to 50 percent of Amazon precipitation being evaporated from the forest (Salati and Vose 1984; Eltahir and Bras 1994; Hutyra et al. 2005). Thus the interception evaporation process is a critical part of the water budget for the Amazon.

Past studies of interception in tropical rain forest sites using the conventional rain-gauge method have yielded a wide range of interception estimates, from 8 to nearly 40 percent of total annual precipitation (Fig. 1). Furthermore, large annual interception differences can be found

within plots in the same forest (Manfroi et al. 2006), interception ranging from 3 to 25 % in 23 subplots over a 4-ha area.
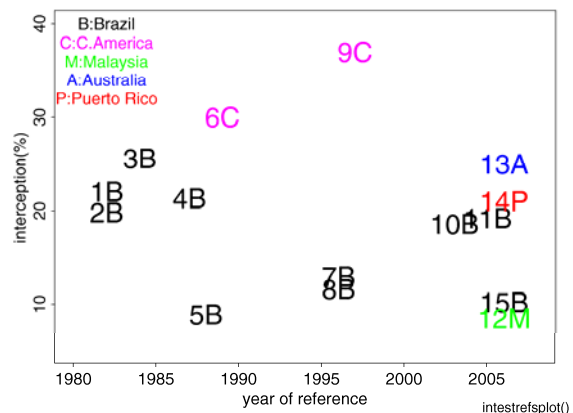

Figure 1: Interception estimates reported in the literature using conventional methods for tropical rain forest sites. Studies done in Brazil are labeled in black with 'B', Central America in pink with 'C', Malaysia in green with 'M', Australia in blue with 'A', and Puerto Rico in red with 'P'. References are as follows: 1B, 2B: Franken et al. (1982a, b); 3B: Schubart et al. (1984); 4B: Leopoldo et al. (1987); 5B: Lloyd and Marques (1988); 6C: Imbach et al. (1989); 7B, 8B: Ubarana (1996); 9C: Cavelier et al. (1997); 10B: Arcova et al. (2003); 11B: Ferreira et al. (2005); 12M: Manfroi et al. (2006); 13A: Wallace and McJannet (2006); 14P: Holwerda et al. (2006); 15B: Germer et al. (2006).

There are now many more long-term eddy flux measurement sites than sites at which the individual forest water budget components (total precipitation, throughfall, and stemflow) are measured. We introduce and describe a new, alternate method for observing interception using eddy-covariance data that could be applied to other tower flux sites worldwide in varying forest types. The approach is to estimate the 'excess' evaporation that occurs during and following

_____
*_Corresponding author address:_ Matthew J. Czikowsky, Atmospheric Sciences Research Center, 251 Fuller Rd., Albany, NY 12203; e-mail: matt@asrc.cestm.albany.edu

individual events, using baseline evaporation time series obtained from long time series of flux data (Fig. 2).
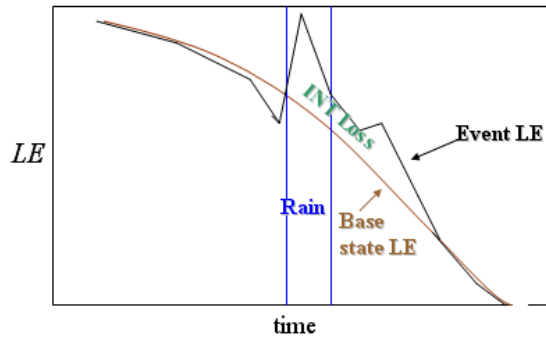

Figure 2: Diagram illustrating the method used to estimate interception using eddy covariance. A base state ensemble LE is composed using dry days. The interception loss for a precipitation event is the difference between the base state and event LE.

One advantage of using the eddy-covariance method over the traditional techniques of estimating interception using rain gauges alone is that the interception evaporation is directly measured and not determined as the residual of incident precipitation and throughfall. Furthermore, the large differences in interception that can occur on a site due to varying forest canopy density, structure and the appearance of canopy gaps is smoothed out using the eddy covariance method as the size of the flux footprint area incorporates these variations, and provides an average interception value over the flux footprint area.

Savenije (2004) argues that there is a broader definition for interception than just the difference between total precipitation and throughfall. Interception also includes the part of the rainfall captured by the ground surface that is evaporated before it can take part in any subsequent runoff, drainage or transpiration processes. The time scales of both of these components of interception evaporation are less than one day. Therefore, traditional interception estimates based on precipitation minus throughfall would be biased low since the wet-surface evaporation contribution to the total interception was neglected. In estimating interception using the eddy covariance method, the total evaporation is measured. Thus, both the interception evaporation contributions from the wet forest canopy and the wet ground surface are included in the measurement.

2. LOCATION AND DATA

The data used in this study were collected in an old-growth forest site that was operated as part of the Large-Scale-Biosphere-Atmosphere Experiment in Amazonia (LBA-ECO, km67 site). This site is located in the Tapajos National Forest south of Santarém, Brazil in the eastern Amazon region (Fig. 3). The site coordinates are 2.88528°S, 54.92047°W at an elevation of 117 m. The height of the forest canopy at the site is approximately 40 m.

An eddy-covariance system that included a Campbell CSAT 3-D sonic anemometer (Campbell Scientific, Inc.) and a Licor 6262 CO_2/H_2O analyzer was operating at a frequency of 8 Hz at a height of 57.8 m, near the top of the flux tower at the km67 site. Net radiation was measured at 64.1 m height using a Kipp and Zonen CNR1 net radiometer, which measured the upward and downward longwave and shortwave radiation
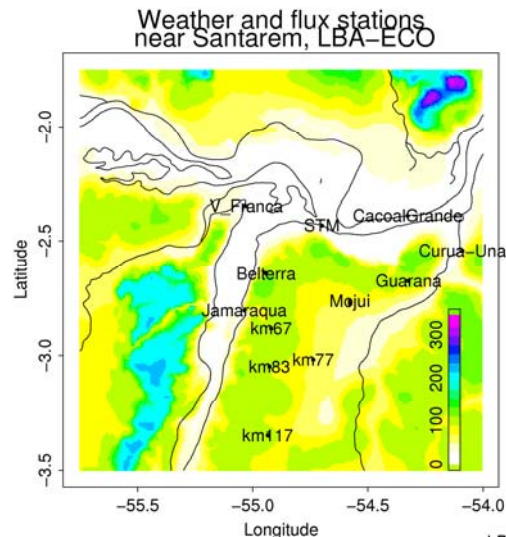

Figure 3: Map of the weather stations and flux-measurement sites operating in the Santarém region (STM) of LBA-ECO. Elevation (m) is shaded. The old-growth forest site where the measurements for the study were taken is denoted as km67 on the map.

components separately. A tipping bucket rain gauge was installed at a height of 42.6 m on the tower, and recorded precipitation at 1-minute intervals with 0.1 mm resolution. A Vaisala CT-25K laser ceilometer was operating at the site from April 2001 to July 2003. Along with cloud base measurements, the ceilometer provided 15-second measurements of a backscatter profile from the surface to 7500 m at 30-m resolution.

Temperature and humidity profile measurements were also taken at eight heights spanning the tower. Further site details can be found in Hutyra et al. (2005).

A large number of precipitation events need to be analyzed under similar conditions for this approach to work. One advantage of using this approach to estimate interception at this site is that there is a marked diurnal pattern in precipitation and cloudiness, especially in the dry season. Precipitation occurs frequently during the same times of the day, helping to build a large ensemble of similar cases. At the km67 site there is an afternoon convective peak in rainfall in both the dry and wet seasons, and a nighttime synoptic peak in the wet season (Fitzjarrald et al. 2008; Fig. 4). Boundary layer cumulus clouds regularly form during the dry season in late morning and dissipate after nightfall (Fig. 5, 6), aiding to form a large ensemble of dry-day latent heat flux. Furthermore, there is little day-to-day variation in cloud fraction and cloud base during the dry season (Fig. 5, 6).
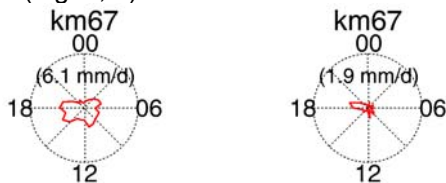

Figure 4: Rain dials for the km67 site during the wet season (left) and dry season (right). Times listed on the rain dials are in GMT (LT + 4 hours).
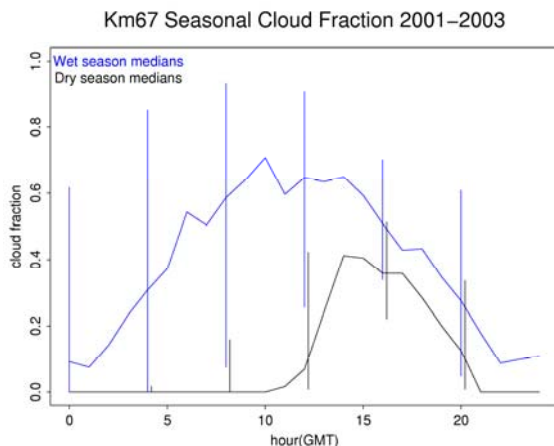

Figure 5: Median cloud cover fraction at km67 by hour of day for the wet season (February through May, plotted in blue) and the dry season (September through December, plotted in black) for 2001 to 2003. The quartiles are indicated by the bars. Note the presence of convective cloudiness during the day in the dry season and the absence of clouds at night in the dry season. Cloud cover fraction peaks during the morning in the wet season.
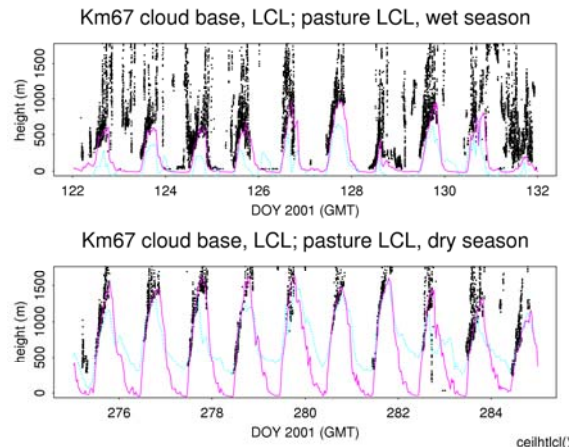

Figure 6: Top panel: Cloud base at km67 (black), lifting condensation level (LCL) at km67 (blue), and LCL at km77 (pink) during a wet season period in 2001 (May 2-11, days 122-131). Bottom panel: As in top panel but for a dry season period in 2001 (October 2-12, days 275-285).

3. METHODS

3.1 Identification of rainfall events

Precipitation events were identified two ways: using the rain gauge and the ceilometer backscatter profile. First, a storm separation time needed to be chosen so that a clear start and end time could be defined for each rainfall event. This is important because a rainfall event is often composed of many nonconsecutive, irregularly-spaced rainfall tips. The length of the storm separation time should be long enough that the precipitation event has finished and the canopy has ample time to dry (provided it is daytime). The storm separation time should not be too long as to combine rainfall of two separate events if the canopy had dried in the interim. We chose a 4-hour storm separation time in our analysis, a value successfully used by Wallace and McJannet (2006) in an Australian rain forest and Van Dijk et al. (2005) in a West Javan rain forest. This separation time worked well at this site given the regularity of the daily timing of the precipitation at this site.

From the 1-minute precipitation data from the rain gauge, a precipitation event was identified in

the following manner. The precipitation file was scanned until the first rain tip was found, which constituted the rain event start time. The rain event end time was defined as the time that a rain tip was reached where there were no further tips for the following 4 hours. This process was repeated for all rain events.

Ceilometers have been used to observe boundary-layer aerosols (Zephoris et al. 2005). We found that the ceilometer is also able to detect rain droplets quite well through the use of the ceilometer backscatter profile (Fig. 7). Due to the large amounts of data contained in each backscatter profile, we averaged the raw 15-second ceilometer data to 5 minutes to perform the rain-identification analysis. This had little impact on the event fluxes calculated later since the minimum flux-calculation length used was 15 minutes.
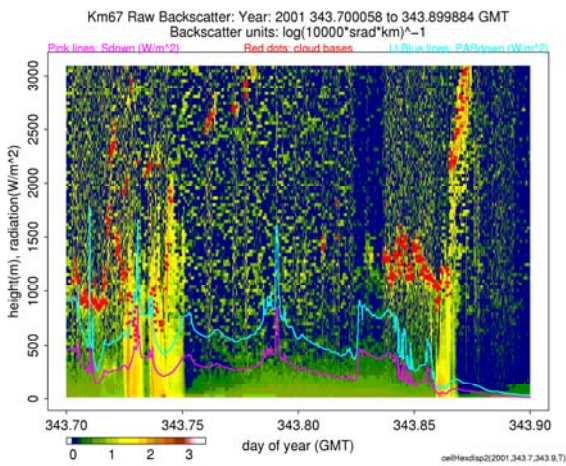

Figure 7: Raw ceilometer backscatter (15-second samples) from 1300 to 1800 LT on December 10, 2001 at the LBA Km67 site. Backscatter units are $log(10000*srad*km)^{-1}$. Red dots indicate cloud bases (m). The pink line is the incoming shortwave radiation (Sdown, units of Wm^{-2}). The light blue line is the photosynthetically active radiation (PARdown, units of Wm^{-2}). Precipitation fell during two periods. The first event occurred in the early afternoon from 1325 to 1400 LT. A second, lighter rain shower occurred for a brief period from 1640 to 1655 LT. The on-site rain gauge recorded 0.762 mm of precipitation for the first rain event, but none for the second rainfall.

The same storm separation time and scanning method were used with the ceilometer data as with the rain gauge data, but two

additional things needed to be determined. These were the threshold value for precipitation, and the heights at which to average the backscatter profile. Based on the review of many days of rainfall, possible values for the rain identification threshold were between 1.2 and 1.5 (units are $log(10000*srad*km)^{-1}$). Histograms of backscatter intensity showed the largest decrease in the number of observed backscatter intensities between 1.2 and 1.3 (not shown). This is an indicator of the rain threshold, since most of the time it is not raining. The rain threshold value of 1.3 $log(10000*srad*km)^{-1}$ was chosen because of the result of the histogram analysis and for the reason that this value agreed best with visual inspection of the ceilometer records for rainfall. A plot of ceilometer backscatter data with the range of rain-identification thresholds and rain gauge data is shown in figure 8.
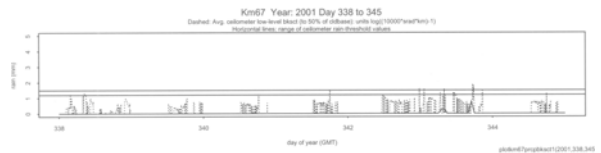

Figure 8: Rainfall (mm, solid line at bottom), and average ceilometer backscatter up to half of the cloud base height (units of $log(10000*srad*km)^{-1}$, dashed line) for days 338 to 345 in 2001. The horizontal solid lines indicate the range of rain-identification threshold values used for the ceilometer backscatter data.

Before the ceilometer data could be used for identifying rainfall events, the range of backscatter profile heights to average needed to be determined. We averaged the ceilometer backscatter profile three ways. First, the lowest 90 m (three range gates) of the backscatter profile were averaged. Second, the backscatter profile was averaged from the lowest level to 50 percent of the cloud base height. Third, the backscatter profile was averaged from the lowest level to 75 percent of the cloud base height. Using the lowest 90 m only for the average backscatter led to false rainfall returns due to fog or smoke. Using the backscatter profile averaged to 75 percent of the cloud base height also led to false rainfall returns due to clouds. Averaging the backscatter profile up to 50 percent of the cloud base height yielded the best results.

One advantage of using the both the ceilometer backscatter data and rain gauge to identify precipitation events over the rain gauge

alone is that that ceilometer detects all rainfall events, including light ones when the rain gauge may not catch any rainfall or not enough to force a tip. Second, the ceilometer gives the instantaneous start time for rainfall, whereas with the tipping bucket rain gauge, light precipitation may have been falling for several minutes before a tip is recorded.

A total of over 200 events were identified using the tipping bucket rain gauge over the April 2001 to July 2003 time period (Table 1). The on-site ceilometer detected nearly 40 light precipitation cases in the dry season that were not detected by the tipping bucket rain gauge.

	Wet	Dry	All
Tipping Bucket (2001-03)	143	63	206
Ceilometer (2001-02)	80	102	182

Table 1: Precipitation events with available data by season. The wet season is defined as the months January through June, the dry season July through December. Both daytime and nighttime events are included.

3.2 Flux calculation methods and ensemble formation

The latent heat flux *LE* and the sensible heat flux *H* were determined by the eddy covariance method using the following:

$$LE = \overline{\rho L_v w'q'} \qquad (1)$$
$$H = \overline{\rho C_p w'T'} \qquad (2)$$

where L_v is the latent heat of vaporization, C_p the specific heat of air, and ρ the air density; $\overline{w'q'}$ and $\overline{w'T'}$ are the latent and sensible kinematic heat fluxes, and the overbars indicate Reynolds averaging.

Four mean-removal methods were initially employed in the analysis: block-average, linear trend removal, centered running mean removal, and smoothed mean removal. These methods have been used in standard practice in the flux measurement community, including over flux tower-measurement networks such as AmeriFlux (e.g. Massman et al. 2002). The block average, linear trend, and centered running mean removal

calculations follow that of Sakai et al. (2001); see also Kaimal and Finnigan (1994). The smoothed mean removal employed here uses a locally-weighted regression smoothing function, run in the Splus software package as the function *supsmu* (Mathsoft, Inc.; function details given in Fitzjarrald et al. 2001) to detrend the time series.

Raw data points that were recorded during calibration cycles, data points out of range for the sonic anemometer, and points with missing data were flagged as spike points. A spike cutoff was set up where any flux-calculation period with greater than 2 percent of its raw data points as spikes was discarded from the analysis.

The sensible and latent heat fluxes ultimately used in the analysis are the average of the smoothed mean removal, linear trend removal, and running mean removal methods. The block-averaged method was too sensitive to the spike points in the data, whereas the other three methods were much more robust with regards to these periods.

Fluxes were initially calculated at 15-minute and 30-minute intervals. The 15-minute fluxes were used for further analysis for two reasons. First, the 30-minute fluxes are insufficient to fully resolve event detail, given the transient nature of the evaporation pulses that occur during a precipitation event. Second, larger quantities of good data were lost surrounding calibration periods when 30-minute fluxes were used as opposed to 15-minute fluxes.

For each 15-minute period the friction velocity u_* was calculated along with the mean and standard deviations of the net radiation $-Q^*$, wind speed, temperature, and humidity. The biomass and canopy air storage term S_{bc} in the energy balance was calculated following the empirical relation of Moore and Fisch (1986) developed in a similar rain forest setting in Manaus, Brazil. The same relation was also used by da Rocha et al. (2004) at a rain forest site (km83 site of LBA-ECO) near the location of this study. The S_{bc} term was calculated as:

$$S_{bc}=16.7\Delta T_r + 28.0\Delta q_r + 12.6\Delta T_r^* \qquad (3)$$

where ΔT_r: hourly air temperature change (C)
Δq_r: hourly specific humidity change (g/kg)
ΔT_r^*: 1-hour lagged hourly air temperature change (C)

Two flux datasets were created, each using different sets of starting and ending times for the flux-calculation periods. In the first dataset, fluxes were calculated for consecutive 15 minute periods for the entire dataset, with the first calculation period of each day beginning at midnight, regardless of the occurrence of precipitation events. This flux dataset was used in the composition of the baseline ensembles. The baseline ensembles for *LE, H, -Q** and S_{bc} are shown in figure 9.

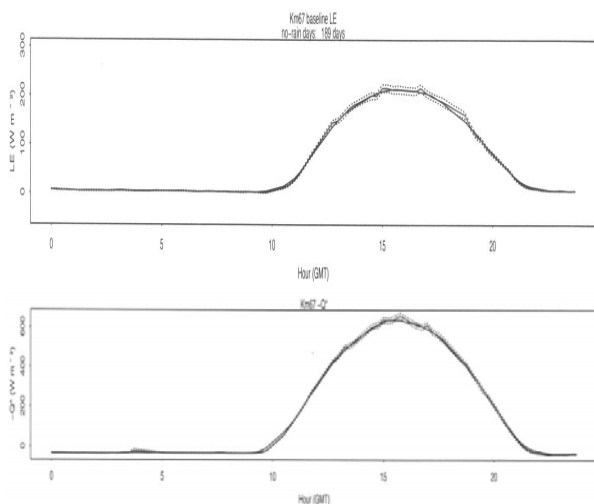Figure 9:(top) Km67 ensemble mean LE for dry days. (Bottom): Km67 ensemble mean –Q* for dry days. The standard errors are dashed. The number of days included in the ensemble is 189.

In the second dataset, fluxes were calculated relative to the timing of each precipitation event. The starting flux-calculation time *t=0* for a given precipitation event depended on the manner which the event was detected. For rain-gauge recorded events, *t=0* was the time of the first recorded tip by the tipping bucket rain gauge. For ceilometer-detected events, *t=0* was the time of the first ceilometer backscatter return detected that was beyond the threshold backscatter value. For events detected by both the rain gauge and the ceilometer, the rain gauge event times were used. Fluxes were calculated at consecutive 15-minute intervals for each event starting four hours before the start of the event until four hours after the end of the event, which was defined as the time of the last recorded tip by the rain gauge or the last detected above-threshold ceilometer backscatter return. The precipitation event flux ensembles were calculated using this dataset.

3.3 Nighttime rainfall event methods

For nighttime cases, the situation is simpler because the base state LE is zero at night (Fig. 10). Therefore, the nighttime portion of event LE can be integrated directly and converted to an equivalent water depth. The remaining amount of water stored in the canopy that does not get evaporated the night of the event will evaporate the following morning, and this portion has to be addressed separately.
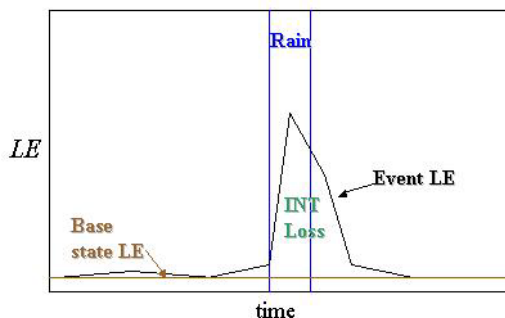

Figure 10: Diagram illustrating the method used to determine nighttime interception losses.

The individual event departures from the base state LE (the interception losses) were used to form an ensemble average of interception evaporation occurring during nighttime rainfall events with respect to the starting time of each rain event.

3.4 Individual daytime event LE baseline determination

For daytime events, the process of determining the interception evaporation is more complex because the base state LE is not zero during the daytime (Fig. 2). To determine the baseline dry-day LE for an individual daytime rainfall event, the net radiation must be taken into account. The net radiation for a given rainfall event is less than what would be observed on a dry day at the same time of day (Fig. 11). The dry-day baseline LE should represent the latent heat flux that would occur on a dry day under the same radiative conditions as a day with rain. Three methods are outlined below to determine the dry-day baseline LE. All methods start with the ensemble LE for all dry days ($[LE]_{dry}$).

Method 1: Divide the dry-day ensemble LE ($[LE]_{dry}$) by the dry-day ensemble $-Q^*$ ($[-Q^*]_{dry}$) to get the dry-day ensemble evaporative fraction ($[EF]_{dry}$) for the corresponding time of day covering the precipitation event. Then for each data point during the event, multiply the dry-day ensemble evaporative fraction by the event $-Q^*$ ($-Q^*_{ev}$) to arrive at the baseline LE:

$$[LE]_{baseline} = [EF]_{dry} * -Q^*_{ev} \qquad (4)$$

Method 2: Divide the dry-day ensemble LE ($[LE]_{dry}$) by the dry-day ensemble $-Q^*$ ($[-Q^*]_{dry}$) to get the dry-day ensemble evaporative fraction ($[EF]_{dry}$) for the corresponding time of day covering the precipitation event. Then for each data point during the event, multiply the dry-day ensemble evaporative fraction by the rain-day ensemble $-Q^*$ ($[-Q^*]_{rain}$) for the same time of day to arrive at the baseline LE:

$$[LE]_{baseline} = [EF]_{dry} * [-Q^*]_{rain} \qquad (5)$$

Method 3: Divide the mean of the event $-Q^*$ ($-Q^*_{ev}$) by the mean of the dry-day baseline $-Q^*$ ($[-Q^*]_{dry}$) for the time of day of the precipitation event to get the radiative fraction ($-Q^*_{frac}$) for the corresponding time of day covering the precipitation event. Multiply this event radiative fraction by the raw dry-day baseline LE ($[LE]_{dry}$) for the same time of day to get the baseline LE:

$$-Q^*_{frac} = (\sum (-Q^*_{ev}) / n_{ev}) / (\sum ([-Q^*]_{dry}) / n_{dry}) \qquad (6)$$

$$[LE]_{baseline} = -Q^*_{frac} * [LE]_{dry} \qquad (7)$$

Applying all three methods to the individual daytime precipitation events, it was found that Method 3 most effectively separated the interception LE from the base-state LE. Method 3 was used in the further analysis.
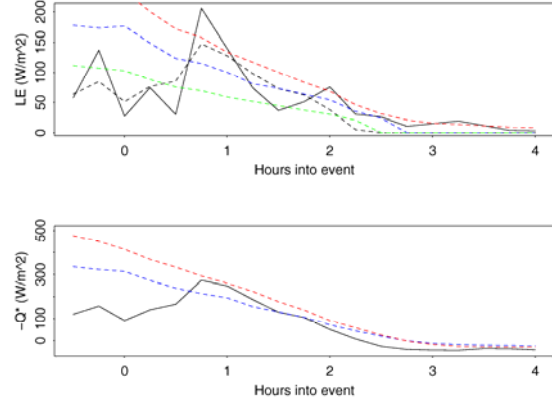

Figure 11: Top: Precipitation event LE (W m^{-2}, solid black line), dry-day ensemble LE (red dashed line), corrected dry-day baseline LE using method 1 (black dashed line), method 2 (blue dashed line), and method 3 (green dashed line). Bottom: Precipitation event $-Q^*$ (W m^{-2}, solid black line), dry-day ensemble $-Q^*$ (red dashed line), and rain-day ensemble $-Q^*$ (blue dashed line).

4. PRELIMINARY RESULTS

4.1 Nighttime precipitation events

For the nighttime precipitation events, ensemble means of the latent heat flux based on the rain start-time show a pulse of interception evaporation starting as the precipitation begins to wet the forest canopy, even before the first recorded tip at *t=0* of the rain events (Fig. 12).
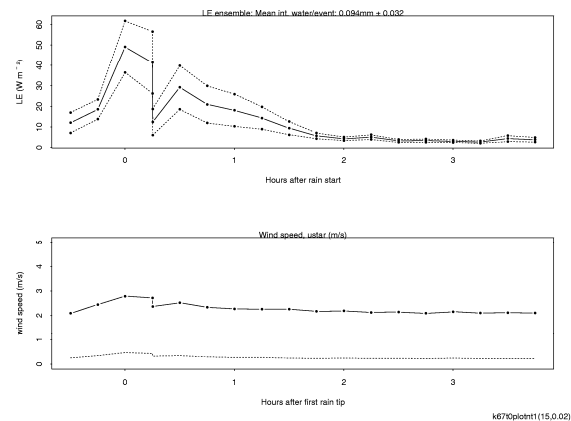

Figure 12: Top panel: Ensemble mean latent heat flux (W m^{-2}) for all 54 nighttime precipitation events. Dotted lines indicate the standard error.

The time axis refers to the number of hours before/after the first rain tip. Bottom panel: Mean wind speed (m/s, solid line) and u* (m/s, dotted line) for the same 54 nighttime precipitation events. The mean interception (± standard error) for these events is 4.72% ± 0.93%. The mean precipitation (± standard error) for these events is 3.32mm ± 0.59mm. The mean amount of water intercepted per event (± standard error) is 0.094mm ± 0.032mm.

The nighttime interception evaporation pulse continues for about two hours following the event start, decreasing in magnitude with time. In the two hours following the precipitation event start, the mean interception estimate was just under 5% of the total precipitation. Then, the evaporation pulse stopped, due to the stabilizing effect as a result of the nocturnal interception evaporation.
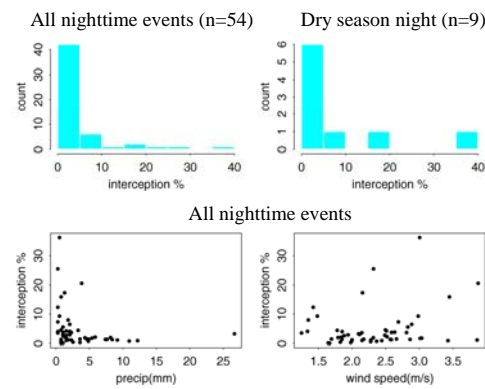

Figure 13: Top left: Histogram of all nighttime rainfall events by interception percentage. Top right: Histogram of all nighttime dry-season rainfall events by interception percentage. Bottom left: Scatterplot of event precipitation (mm) and interception percentage. Bottom right: Scatterplot of wind speed (m s^{-1}) and interception percentage.

A few of the nighttime events were associated with much higher interception estimates of over 15% (Fig. 13). These high-interception nighttime events are broken into two categories. First, there were high-interception, high-wind events occurring around midnight, between 2300LT and 0100LT. Ensemble mean wind speeds for these events reached nearly 5 m/s, (Fig. 14) and agree with the timing of nocturnal squall lines at the site. The second type of high-interception nighttime event is a high-interception, low-wind event that occurs near the time of evening transition (around

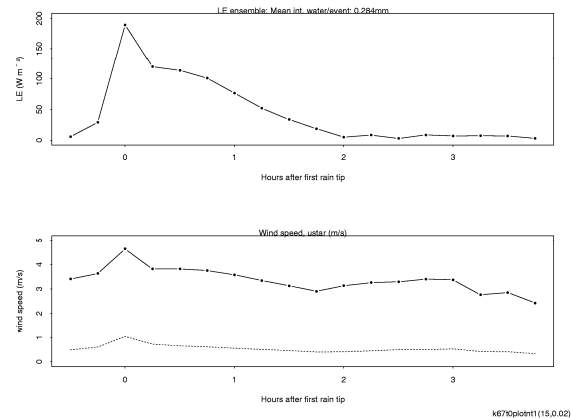1800LT). Wind speeds during these events remain below 3 m/s (Fig. 15).

Figure 14: Top panel: Ensemble mean latent heat flux (W m^{-2}) for the 4 nighttime high-interception, high-wind events. The time axis refers to the number of hours before/after the first rain tip. Bottom panel: Mean wind speed (m/s, solid line) and u* (m/s, dotted line) for the same 4 nighttime precipitation events. The mean interception (± standard error) for these events is 20.6% ± 5.7%. The mean precipitation (± standard error) for these events is 1.40mm ± 0.81mm. The mean amount of water intercepted per event is 0.284mm.
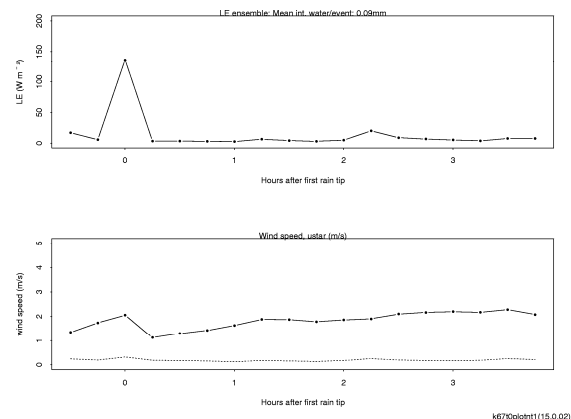

Figure 15: Top panel: Ensemble mean latent heat flux (W m^{-2}) for the 4 nighttime high-interception, low-wind events. The time axis refers to the number of hours before/after the first rain tip. Bottom panel: Mean wind speed (m/s, solid line) and u* (m/s, dotted line) for the same 4 nighttime precipitation events. The mean interception (± standard error) for these events is 16.1% ± 3.6%. The mean precipitation (± standard error) for these events is 0.57mm ± 0.24mm. The mean amount of water intercepted per event is 0.09mm.

capacity value.

4.2 Daytime precipitation events

For the daytime rainfall events, ensembles of departure from baseline LE (representing interception evaporation) were constructed for different classes of rainfall rates with respect to the rain-event starting times. For light-to-moderate rainfall rates (<= 16 mm hr^{-1}), there was a steady pulse of interception evaporation for 4 hours following the event start (Fig. 16), with departure LE values maximizing at around 30 W m^{-2} around the rain-start time for the events.
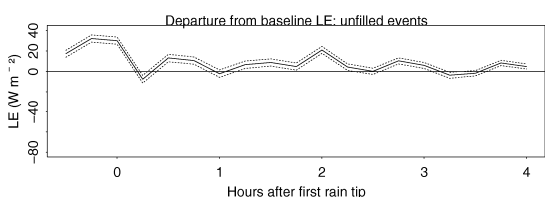

Figure 16: Mean departure from baseline LE (W m^{-2}) for daytime rainfall events with rainfall intensities <= 16 mm hr^{-1} using method 3 (solid black line, standard error dashed). A total of 104 events are included in the ensemble, and missing event data points were filled. The time *t=0* indicates the time of the first recorded tip by the rain gauge for tipping bucket rain gauge-recorded events or the first precipitation echoes detected by the ceilometer for ceilometer-detected events.

For the heavy rainfall-rate events (>16 mm hr^{-1}), the LE departure ensemble (Fig. 17) shows that the eddy-covariance system fails during the first hour after rainfall. However, the system starts working again after the first hour following rainfall, meaning that there is still useful data that can be obtained directly from the eddy-covariance system. During the period when the eddy-covariance system fails, it is necessary to fill in the observed event LE with Penman-Monteith-estimated LE. This is part of the ongoing work.

The mean intercepted water binned by rainfall intensity for daytime events (Fig. 18) shows an increase in the amount of water intercepted per event with increasing rainfall rate (up to 16 mm hr^{-1}). A revised estimate of the high-rainfall-rate interception will be made using the Penman-Monteith-estimated LE when needed while re-analyzing the heavy rainfall events. This will help answer whether the amount of mean intercepted water will continue to increase for the heavy rainfall events or level off towards a canopy-
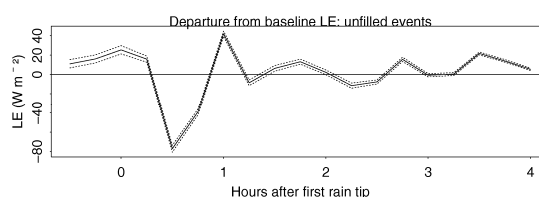

Figure 17: Mean departure from baseline LE (W m^{-2}) for daytime rainfall events with rainfall intensities > 16 mm hr^{-1} using method 3 (solid black line, standard error dashed). A total of 25 events are included in the ensemble, and missing event data points were filled. The time t=0 indicates the time of the first recorded tip by the rain gauge for tipping bucket rain gauge-recorded events or the first precipitation echoes detected by the ceilometer for ceilometer-detected events.
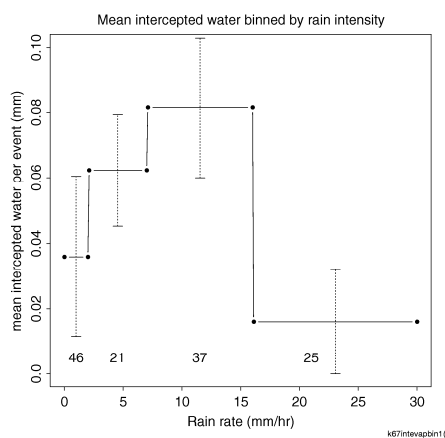

Figure 18: Mean intercepted water binned by rainfall intensity for daytime events, with the standard error bars for each rain intensity bin shown. The rain intensity bins are as follows: <= 2 mm hr^{-1}, 2-7 mm hr^{-1}, 7-16 mm hr^{-1}, and > 16 mm hr^{-1}. The numbers along the bottom of the plot indicate the number of events included in each rain intensity bin.

The mean interception estimate for light rainfall-rate events (<= 2 mm hr^{-1}) was 18% (Table 2), with estimates for moderate rainfall rates (2-16 mm hr^{-1}) decreasing to about 10%. The percentage of daytime light-to-moderate rainfall events in our sample with good data (80.7%) is close to the percentage of all light-to-moderate rainfall events detected in our dataset (77.4%).

Rainfall rate	Mean interception (standard error)	Number of events
<= 2 mm hr^{-1}	18.0% (12.2%)	46
2-16 mm hr^{-1}	9.9% (2.6%)	58
> 16 mm hr^{-1}	NA	25

Table 2: Mean interception estimates for daytime rainfall events classed by rainfall rate.

4.3 Energy balance comparison for dry and rain days

To compare the energy balance components for dry and rain days, ensembles of each of the components –Q*, LE, and H were assembled for dry days (189 days) and days with rain that started after 1400 GMT (100 days total). At the Km67 site, the number of rainfall cases observed starts to increase in the late morning around 1400 GMT, with the greatest number of cases occurring at the afternoon convective peak. Choosing this time effectively separates the rainfalls associated with the nighttime/early morning peak from the afternoon convective peak. In the early morning, before 1200 GMT, -Q* for dry and rain days are close to each other. However, –Q* decreases on the rain days starting around 1200 GMT, about two hours before the rain period on the rain days, and representing the onset of cloudiness (Fig. 19). For the remainder of the day, all of the energy balance components are greater in magnitude for the dry days than the rain days.
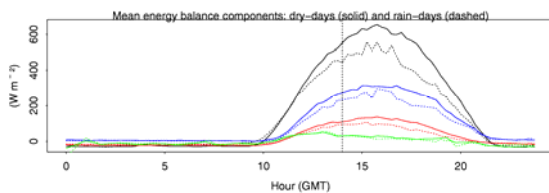
Dividing the energy balance components for the dry and rain days by their respective –Q* values results in energy balance component fractions that can directly be compared for dry and rain days. Once the total radiative energy is taken into account, the effect of the rain on the energy balance components becomes more apparent (Fig. 20). During the early morning pre-rainfall period, the evaporative fraction is greater on the dry days than the rain days. Once the rainfall period is reached, the evaporative fraction becomes greater on the rain days than the dry days and remains so for the balance of the day. During the late afternoon period (1800 – 2200 GMT), the rain-day evaporative fraction is over 5 percent greater than the dry-day evaporative fraction (Table 3). On the rain days, the evaporative fraction increases over 16 percent from the pre-rain period to the late afternoon period, while the sensible heat fraction falls by 7 percent. Most of the energy required for the evaporative fraction increase on the rain days appears to be supplied by the storage term. From the pre-rainfall morning period to the late afternoon period, the storage fraction decreases by over 15 percent, falling to negative values indicating a release of energy. The storage fraction decrease nearly offsets the evaporative fraction increase on the rain-days.
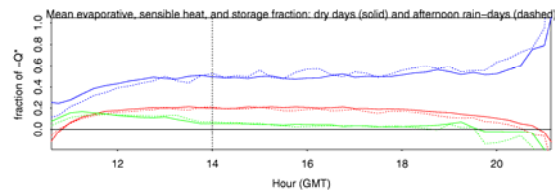

Figure 20: Mean evaporative fraction (blue, top pair of lines), sensible heat fraction (red, middle pair of lines), and storage fraction (green, bottom pair of lines) of –Q* for dry days (solid) and days with rain after 1400 GMT (dashed). The vertical dashed line indicates the 1400 GMT rain cutoff time. There are 189 days included in the dry-day ensemble and 100 days in the rain-day ensemble.

Figure 19: Top: Mean energy balance components for dry days (solid lines) and afternoon rain days (dashed lines). –Q* is in black (top pair of lines), LE in blue (second pair of lines from top), H in red (third pair of lines from top), and S_{bc} in green (bottom pair of lines). The dry-day ensemble includes 189 days, with 100 days in the rain-day ensemble. The vertical dashed line indicates the time (1400 GMT) after which rain fell during the rain days.

	1200 – 1400 GMT		1400 – 1800 GMT		1800 – 2200 GMT	
	Dry	Pre-rain	Dry	Rain	Dry	Rain
[LE] / [-Q*] (%)	47.5	44.4	49.3	51.8	55.5	60.7
[H] / [-Q*] (%)	19.9	18.3	20.3	18.7	14.6	11.3
[Sbc] / [-Q*] (%)	10.2	11.8	4.3	4.3	0.0	-3.5

Table 3: Mean evaporative, sensible heat, and storage fractions of –Q* for dry and rain days for the pre-rain period 1200 – 1400 GMT and rain periods 1400 – 1800 GMT and 1800 – 2200 GMT.

Bowen ratio values during the pre-rainfall morning period are nearly the same for the dry and rain days (Fig. 21). Following the onset of rainfall, the rain-day Bowen ratio becomes lower than the dry-day Bowen ratio and remains so for the rest of the day. For the period following rainfall (1400 GMT – 2100 GMT), mean Bowen ratios for the dry and rain days are 0.34 and 0.28 respectively.
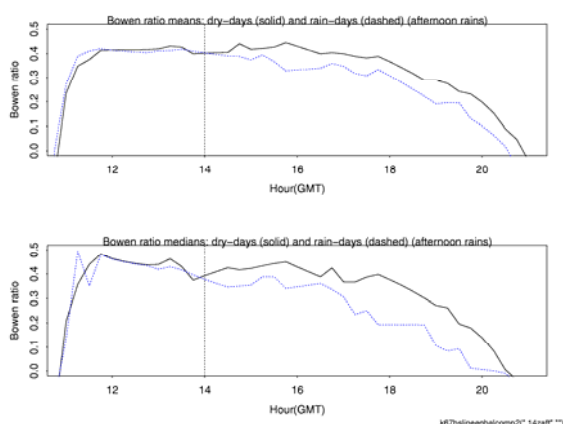

Figure 21: Top: Mean Bowen ratio for dry days (solid black line) and days with rain after 1400 GMT (dashed blue line). The vertical dashed line indicates the 1400 GMT rain cutoff time. Bottom: Same as top but Bowen ratio medians are plotted.

5. SUMMARY AND CONTINUING/FUTURE WORK

We have introduced a methodology by which one can directly observe the amount of interception evaporation using eddy-covariance data that are available at a number of worldwide flux tower sites. Tests of the method over an eastern Amazon old-growth rain forest show the method to be effective under light-to-moderate rainfall rates (<= 16 mm hr^{-1}). For events with heavy rainfall rates (> 16 mm hr^{-1}), Penman-Monteith estimated evaporation can be used to substitute for LE during periods when the eddy-covariance does not work, and these estimates comprise part of the continuing work.

Mean interception for moderate daytime rainfall events was about 10%, with light events at 18%. Energy balance comparisons between dry and afternoon rain-days show an approximately 15% increase of evaporative fraction on the rain days, with the energy being supplied by a nearly equivalent decrease in the canopy heat storage.

Future work includes testing of the method at other flux-tower sites with different land cover types. Furthermore, on-site comparisons between this method and conventional interception-estimation methods would be useful.

6. ACKNOWLEDGEMENTS

7. REFERENCES

Arcova, F., V. de Cicco, and P. Rocha, 2003: Precipitacão efetiva e interceptacão das chuvas por floresta de Mata Atlântica em uma microbacia experimental em Cuhnha-São Paulo. *R. Avore, Vicosa*-MG, **27**, 257-262.

Cavelier, J., M. Jaramillo, D. Solis, and D. de Leon, 1997: Water balance and nutrient inputs in bulk precipitation in tropical montane cloud forest in Panama. *J. Hydrol.*, **193**, 83-96.

Da Rocha, H. R., M. L. Goulden, S. D. Miller, M. C. Menton, L. D. V. O. Pinto, H. C. de Freitas, A. M. S. Figueira, 2004: Seasonality of water and heat fluxes over a tropical forest in eastern Amazonia. *Ecol. Appl.*, **14**, S22-S32.

Ferreira, S., F. Luizao, and R. Dallarosa, 2005: Precipitacão interna e interceptação da chuva em floresta de terra firme submetida a extracão seletiva de madeira na Amazonia Central. *Acta Amazonica*, **35**, 55-62.

Fitzjarrald, D. R., O. C. Acevedo, and K. E. Moore, 2001: Climatic consequences of leaf presence in the eastern United States. *J. Climate*, **14**, 598-614.

Fitzjarrald, D. R., R. K. Sakai, O. L. L. Moraes, R. C. Oliveira, O. C. Acevedo, M. J. Czikowsky, and T. Beldini, 2008: Spatial and temporal rainfall variability near the Amazon-Tapajós confluence. Submitted to *J. Geophys. Res – Biogeosciences*.

Franken, W., P. Leopoldo, E. Matsui, and M. Ribeiro, 1982a: Interceptacão das precipitacoes em floresta amazonica de terra firme. *Acta Amazonica*, **12**, 15-22.

Franken, W., P. Leopoldo, E. Matsui, and M. Ribeiro, 1982b: Estudo da interceptacão da agua de chuva em cobertura florestal amazonica do tipo terra firme. *Acta Amazonica*, **12**, 327-331.

Germer, S., H. Elsenbeer, and J. Moraes, 2006: Throughfall and temporal trends of rainfall redistribution in an open tropical rainforest, SW Amazonia (Rodônia, Brazil). *Hydrol. Earth Syst. Sci.*, **10**, 383-393.

Hewlett, J. D., 1982. Principles of Forest Hydrology. The University of Georgia Press, Athens, GA, 183 p.

Holwerda, F., F. Scatena, and L. Bruijnzeel, 2006: Throughfall in a Puerto Rican montane rainforest: a comparison of sampling strategies. *J. Hydrol.*, **327**, 592-602.

Hutyra, L. R., J. W. Munger, C. A. Nobre, S. R. Saleska, S. A. Vieira, and S. C. Wofsy, 2005: Climatic variability and vegetation vulnerability in Amazonia. *Geophys. Res. Lett.*, **32**, L24712, doi:10.1029/2005GL024981.

Imbach, A., and Coauthors, 1989: Modelling agroforestry systems of cacao (*Theobroma cacao*) with laurel (*Cordia alliodora*) and cacao with poro (*Erthrina poeppigiana*) in Costa Rica IV. Water balances. *Agroforestry Systems*, **8**, 267-287.

Kaimal, J. C., and J. J. Finnigan, 1994: Atmospheric boundary layer flows. Oxford, 289 pp.

Leopoldo, P., W. Franken, E. Salati, and M. Ribeiro, 1987: Towards a water balance in the Central Amazonian region. *Experientia*, **43**, 222-233.

Lloyd, C., and A. Marques, 1988: Spatial variability of throughfall and stemflow measurements in Amazonian forest. *Agric. For. Meteor.*, **42**, 63-73.

Manfroi, O., and Coauthors, 2006: Comparison of conventionally observed interception evaporation in a 100-m^2 subplot with that estimated in a 4-ha area of the same Bornean lowland tropical forest. *J. Hydrol.*, **329**, 329-349.

Massman, W. J., and X. Lee, 2002: Eddy covariance flux corrections and uncertainties in long-term studies of carbon and energy exchanges. *Agric. For. Meteor.*, **113**, 121-144.

Moore, C. J., and G. F. Fisch, 1986: Estimating heat storage in Amazonian tropical forest. *Agric. For. Meteor.*, **38**, 147-168.

Newson, M. D., and I. R. Calder, 1989: Forests and water resources: problems of prediction on a regional scale. *Phil. Trans. Roy. Soc. London.* B **324**, 283-298.

Sakai, R. K., D. R. Fitzjarrald, and K. E. Moore, 2001: Importance of low-frequency contributions to eddy fluxes over rough surfaces. *J. Appl. Meteor.*, **40**, 2178-2192.

Salati, E., and P. B. Vose, 1984: Amazon Basin: A system in equilibrium. *Science*, **225**, 129-138.

Savenije, H. H. G., 2004: The importance of interception and why we should delete the term evapotranspiration from our vocabulary. *Hydrological Processes*, **18**, 1507-1511.

Schubart, H., W. Franken, and F. Luizao, 1984: Uma floresta sobre solos pobres. *Ciencia Hoje*, **2**, 26-32.

Stewart, J. B., 1977: Evaporation from the wet canopy of a pine forest. *Water Resour. Res.*, **13**, 915-921.

Ubarana, V., 1996: Observation and modelling of rainfall interception loss in two experimental sites in Amazonian forest. *Amazonian deforestation and climate*, Chichester, John Willey, 151-162.

Van Dijk, A., A. Meesters, J. Schellekens, and L. Bruijnzeel, 2005: A two-parameter exponential rainfall depth-intensity distribution applied to runoff and erosion modeling. *J. Hydrol.*, **330**, 155-171.

Wallace, J., and D. McJannet, 2006: On interception modelling of a lowland coastal rainforest in northern Queensland, Australia. *J. Hydrol.*, **329**, 477-488.

Zephoris, M., H. Holin, F. Lavie, N. Cenac, M. Cluzeau, O. Delas, F. Eideliman, J. Gagneux, A. Gander, and C. Thibord, 2005: Ceilometer observations of aerosol layer structure above the Petit Luberon during ESCOMPTE's IOP 2. *Atmos. Research*, **74**, 581-595.